Heat risk assessment using surrogate model for meso-scale surface temperature

Byeongseong Choi
Department of Civil and Environmental Engineering
Carnegie Mellon University
Pittsburgh, PA 15213
byeongsc@andrew.cmu.edu

Matteo Pozzi
Department of Civil and Environmental Engineering
Pittsburgh, PA 15213
mpozzi@cmu.edu

Mario Berges
Department of Civil and Environmental Engineering
Pittsburgh, PA 15213
marioberges@cmu.edu

Abstract

Cities are vulnerable to heat-induced risks due to their dense population and their characteristically higher temperature (as compared to the surrounding environment). Therefore, fast/accurate heat risk assessment is desired for mitigation plans and sustainable community management. This paper introduces a probabilistic model to forecast the meso-scale surface temperature in an urban area at a relatively low computational cost, as an alternative to widely-utilized but computationally-intensive Numerical Weather Prediction (NWP) models. After calibrating the model with data from two urban areas, we assess the model's prediction performance. During our numerical test, the model's 3hours-ahead prediction error is evaluated as 0.99-1.59°C in root-mean-squared error (RMSE) and 0.94-0.96 in correlation coefficient (r), which is comparatively better performance than a baseline model. Finally, we integrate the developed model into a probabilistic risk analysis framework to estimate extreme temperature distribution around these cities. In doing so, we expand the model's applicability, providing insights on the future risk and enabling various other statistical inferences. As a result of risk assessment, a posterior probability map is provided as the risk of extreme temperature during the test period, and the occurrence rate of urban heat island is evaluated for both urban areas.

1 Introduction

Surface temperature has a broad impact on human health and activity, and extreme heatwaves are one of the deadliest hazards around the globe (Changnon et al. (1996)). Urban areas are particularly vulnerable to heat stressors because of their high population density. An apparent heat pattern in an urban area, known as the Urban Heat Island (UHI) effect, is its trapped heat within the building canopy resulting in higher temperatures than the surrounding environment. The UHI phenomenon has a non-linear relationship with extreme heatwaves making assessments of heat risks especially

Workshop on machine learning for engineering modeling, simulation and design @ NeurIPS 2020

challenging.
This paper introduces a spatio-temporal surrogate model that predicts surface temperature for the 150km∼200km meso-scale domain (at a 1km resolution). We then suggest using this surrogate model to quantify the urban heat risk that would not be directly observable from the data. In the following sections, the term 'surface temperature' is used to denote '2m temperature' – that is, the temperature at 2m above the ground. That is because 2m temperature influences human comfort and mortality more than strictly defined 'surface temperature' (Anderson and Bell (2009) and Voogt and Oke (2003)).

1.1 Numerical weather prediction

Numerical weather prediction (NWP) is the golden-standard for current weather forecast and research (Weyn et al. (2019)). NWP is based on numerical models that solve differential equations related to physical processes in atmospheric science. NWP has improved its accuracy through advances in computing resources. For example, the Princeton Urban Canopy Model captures the complicated heat patterns in an urban area, with a bias as small as 0.4∼1.1°C, by incorporating Weather Research and Forecasting Model (WRF-PUCM) (Li and Bou-Zeid (2014)). Still, the main challenge of NWP is its high computational cost, which limits its applicability for heat risk assessments that are time-sensitive.

1.2 Probabilistic approach

Probabilistic approaches, such as the one presented in this paper, aim to characterize the complex spatio-temporal process with statistical descriptions. For example, Berliner et al. (2000)) proposed a Bayesian hierarchical model to estimate the monthly sea-surface temperature for the tropical Pacific region (Berliner et al. (2000) and Cressie and Wikle (2015)). Similarly, Malings et al. (2017) suggested using a Gaussian process (GP) to approximate the urban surface temperature and used this model to optimize the sensing locations over a city (Malings et al. (2018)), via a Value-of-Information analysis. Though related to our objective, these prior efforts have focused primarily on forecasting temperatures without extending it to risk quantification.

2 Surrogate model

We now provide a more formal description of our probabilistic model.

2.1 State-space representation

State-space representations have been widely adopted to characterize complex physical systems/processes, and to estimate their dynamical behavior by incorporating observations in a variety of Kalman Filter/Smoothing schemes (Welch and Bishop (1995)).
In our state-space model, a (high-dimensional) temperature field vector $\mathbf{y}_t$ $(P\times 1)$, is decomposed into three factors: average temperature field $\boldsymbol{\mu}_\tau$, a linear function of the low-dimensional latent states $\mathbf{x}_t$ $(R\times 1; R \ll P)$, and an error term $\mathbf{v}_t$.

$$\mathbf{y}_t = \boldsymbol{\mu}_\tau + \boldsymbol{\Phi}_\tau \, \mathbf{x}_t + \mathbf{v}_t \tag{1}$$

where $\boldsymbol{\Phi}_\tau$ and $\boldsymbol{\mu}_\tau$ are the embedding matrix and the average field, respectively, that are time-dependent parameters according to the time of the day τ, discretized into 48 steps from 00:00 (i.e., midnight) to 23:30. Note that τ is really a function of time t (i.e., $\tau(t)$) but for notational conveniece we omit this. The temporal evolution for the process is assumed to be Markovian with the linear transition matrix $\mathbf{F}_\tau$ that also depends on the time of the day τ.

$$\mathbf{x}_t = \mathbf{F}_t \mathbf{x}_{t-1} + \mathbf{w}_t = \mathbf{F}_\tau \, \mathbf{x}_{t-1} + \mathbf{w}_t \tag{2}$$

where $\mathbf{w}_t$ the zero-mean Gaussian noise at time t, whose covariance matrix $\boldsymbol{\Sigma}_{\mathbf{w}}^{\tau}$ is also a function of τ. Fig 1 summarizes the overall hierarchical structure of the proposed model.

2.2 Latent variable selection

We choose the state variables as the observable temperature at certain locations where most information exists to estimate the rest of the field variables. Selecting such locations, denoted as a set $\mathcal{A}$,

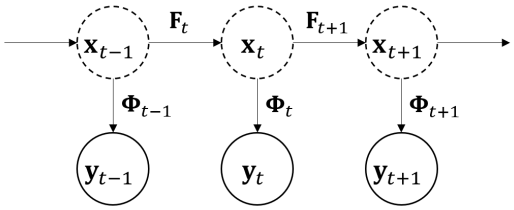

Figure 1: Graphical representation of the proposed model

then becomes an optimal sensor placement problem. We partition the field of residual temperature $\tilde{\mathbf{y}}_t$ into two sub-vectors $\mathbf{y}_t^{\text{ip}}$ and $\mathbf{x}_t$ where the vector $\tilde{\mathbf{y}}_t$ is the difference between temperature $\mathbf{y}_t$ and its corresponding mean-field $\boldsymbol{\mu}_\tau$.

$$\tilde{\mathbf{y}}_t = \mathbf{y}_t - \boldsymbol{\mu}_\tau = \begin{bmatrix} \mathbf{y}_t^{\text{ip}} \\ - \\ \mathbf{x}_t \end{bmatrix} \tag{3}$$

To solve the optimal placement problem, we adopt a method proposed in Krause et al. (2008), maximizing the difference between marginal entropy and conditional entropy of the places where no sensor is installed.

$$\mathcal{A}^* = \text{argmax}_{\mathcal{A}\subseteq S:|\mathcal{A}|=R} \left[H\left(\mathbf{y}_t^{\text{ip}}\right) - H\left(\mathbf{y}_t^{\text{ip}}|\mathbf{x}_t\right) \right] \tag{4}$$

$|\mathcal{A}|$ is the number of sensor placements, which is equal to the dimension of latent variables R. $\mathcal{S}$ is a set of locations where we can place sensors. $H(\cdot)$ is the entropy or conditional entropy. A merit of this approach is that the latent variables are directly observable from the data.

2.3 Parameter estimation

After selecting the optimal location $\mathcal{A}^*$, the transition matrix is calibrated, adopting the least square error loss function (LSE) with a regularization term.

$$\mathcal{L} = \sum_\tau \left[\frac{1}{2N_D} \sum_{\{t|\text{HoD}(t)=\tau\}} \|\mathbf{x}_t - \mathbf{F}_\tau \, \mathbf{x}_{t-1}\|_{L_2}^2 \right] + \frac{1}{2}\alpha_{\text{HM}} \sum_\tau \|\mathbf{F}_\tau - \mathbf{F}_{\text{HM}}\|_2 \tag{5}$$

where $\text{HoD}(\cdot)$ returns the hour of the day with the input t, i.e. $\tau = \text{HoD}(t)$, and $\|\cdot\|_2$ is the Frobenius norm. $\mathbf{F}_{\text{HM}}$ is a homogeneous transition matrix that is obtained through a pre-training procedure.

$$\mathbf{F}_{\text{HM}} = \mathbf{\Sigma}^{\text{HM}}_{\mathbf{x}_t\mathbf{x}_{t-1}} \left[\mathbf{\Sigma}^{\text{HM}}_{\mathbf{x}_t\mathbf{x}_t} + \eta_{\text{HM}}\mathbf{I} \right]^{-1} \tag{6}$$

where $\mathbf{\Sigma}^{\text{HM}}_{\mathbf{x}_t\mathbf{x}_{t-1}}$ and $\mathbf{\Sigma}^{\text{HM}}_{\mathbf{x}_t\mathbf{x}_t}$ are the covariance matrices that is constructed by using the following stationary and isotropic kernel functions. η_{HM} is a hyper-parameter that prevents $\mathbf{F}_{\text{HM}}$ from being a typical identity matrix, forcing a geometrically closer predictor to have an larger absolute value, which is set to be 0.1°C.

$$\mathbf{\Sigma}^{\text{HM}}_{\mathbf{x}_t\mathbf{x}_t}(i,j) = \sigma \text{exp}\left[-\frac{\Delta_{i,j}}{\lambda_{\text{HM}}} \right], \;\; \mathbf{\Sigma}^{\text{HM}}_{\mathbf{x}_t\mathbf{x}_{t-1}} = \rho \mathbf{\Sigma}^{\text{HM}}_{\mathbf{x}_t\mathbf{x}_t} \tag{7}$$

where $\mathbf{\Sigma}^{\text{HM}}_*(i,j)$ is the i-th row and j-th column element of the matrix. σ and ρ are scalar values that represent the homogeneous standard deviation and correlation coefficient, respectively. $\Delta_{i,j}$ is the geometric distance between the sites i and j, and λ_{HM} is a parameter that models the decaying correlation with increasing distance. The pre-training procedure searches the maximum-likelihood estimators for (7). The regularization coefficient α_{HM} is then selected through n-fold cross-validation. Such a regularization term is to find a stable transition by forcing the learned matrix to be similar to the homogeneous matrix. The following loss function provides the estimation for the embedding matrix $\mathbf{\Phi}_\tau$ similarly to (5).

$$\mathcal{L}^\Phi = \sum_\tau \left[\frac{1}{2N_D} \sum_{\{t|\text{HoD}(t)=\tau\}} \|\tilde{\mathbf{y}}_t - \mathbf{\Phi}_\tau \, \mathbf{x}_t\|_{L_2}^2 \right] + \frac{1}{2}\alpha_\Phi \sum_\tau \|\Phi_\tau - \Phi_{\text{HM}}\|_2 \tag{8}$$

Table 1: Summary of training data

Setting	New York	Pittsburgh
Latitude	[40.040, 41.513]° N	[39.546, 41.325]°N
Longitude	[74.701, 72.741]°W	[81.172, 78.777]°W
Spatial grid	159×159	201×198
Grid spacing	1km	1km
Calibration years	2016/2017/2018	2016/2017/2018
Start date	Jun 1 00:00 UTC	Jun 1 00:00 UTC
End date	Sep 1 00:00 UTC	Sep 1 00:00 UTC
Time interval	30min	30min

The homogeneous embedding matrix Φ_{HM} is defined similarly to the homogeneous transition matrix $\mathbf{F}_{\text{HM}}$ sharing the the parameters, λ_{HM}, η_{HM}, and σ.

$$\mathbf{\Phi}_{\text{HM}} = \mathbf{\Sigma}^{\text{HM}}_{\tilde{\mathbf{y}}_t \mathbf{x}_t} \left[\mathbf{\Sigma}^{\text{HM}}_{\mathbf{x}_t \mathbf{x}_t}\right]^{-1} \text{ where } \mathbf{\Sigma}^{\text{HM}}_{\tilde{\mathbf{y}}_t \mathbf{x}_t}(i,j) = \sigma \text{exp}\left[-\frac{\Delta_{i,j}}{\lambda_{\text{HM}}}\right]. \tag{9}$$

3 Model calibration

To calibrate the model, we reanalyzed historical weather data with the WRF-PUCM by down-scaling 6 hourly 12km×12km data of North American Meso-scale Forecast System 12 km Analysis (NAM-ANL; *NCEP North American Mesoscale (NAM) 12 km Analysis* (2015)) to 1km×1km grid data with 30 minutes intervals. Using the simulated data, we calibrate the proposed model for both domains around Pittsburgh (200km×200km) and New York City (160km×160km). Hereafter, the reanalyzed surface temperature by WRF-PUCM is used as a ground truth to the proposed model. Table 1 summarizes the dataset that were used to calibrate the model.

4 Model validation

We validate the model by assessing the prediction performance with the multiple use cases. The use cases are listed as the followings:

Case 1: we exploit local temperature measurements at hypothetical weather stations $y_i(t)$ with the small level of error, zero-mean and 0.1°C standard deviation. The simulated weather stations are assumed to be evenly distributed with 6km spacing.
Case 2: In addition to Case 1, the average temperature over the entire domain is provided for the test period (3 days) with 6 hourly intervals (being updated at 00:00, 06:00, 12:00, 18:00).
Case 3: In addition to Case 1, this case provides average temperatures of multiple square-shape zones (12km ×12km) with 6 hourly intervals for the test period.

Case 2 and 3 describe the use cases when an external NWP provides a coarse resolution solution as an outcome of the broader scale simulation. We set two baselines using the model proposed by Malings et al. (2017). Because of the computational complexity in using the fully-connected GP, we constrain the number of data points to predict the surface temperature of each location.

Baseline 1: We only input the 12km×12km zonal average to the GP model during the test period with 6 hourly intervals.
Baseline 2: In addition to Baseline 1, this case uses field measurements $y_i(t)$ within a radius of 10 km sub-domain at 9 previous timestamps (Current time − [00:00, 00:30, 01:00, 03:00, 06:00, 09:00, 12:00, 18:00, 24:00]).

The short-term forecast is conducted by implementing a Gaussian linear smoother, also known as a Kalman Filter (or smoother) (KF). The KF estimates the state with measurements as described in Barber (2012) and Welch and Bishop (1995). During the forecast procedures, the KF provides the posterior distribution of the temperature field with the observations on field data and the external coarse forecast.
The trained model predicts the reanalyzed surface temperature by WRF-PUCM from 00:00

Table 2: Summary of use cases

	Field measurement		External forecast	
	Grid spacing	Time interval	Zonal scale	Time interval
Case 1	6km	30min	-	-
Case 2	6km	30min	Domain size	6 hourly
Case 3	6km	30min	12km×12km	6 hourly
Baseline 1	12km×12km	6 hourly	12km×12km	6 hourly
Baseline 2	6km (<10km)	various	12km×12km	6 hourly

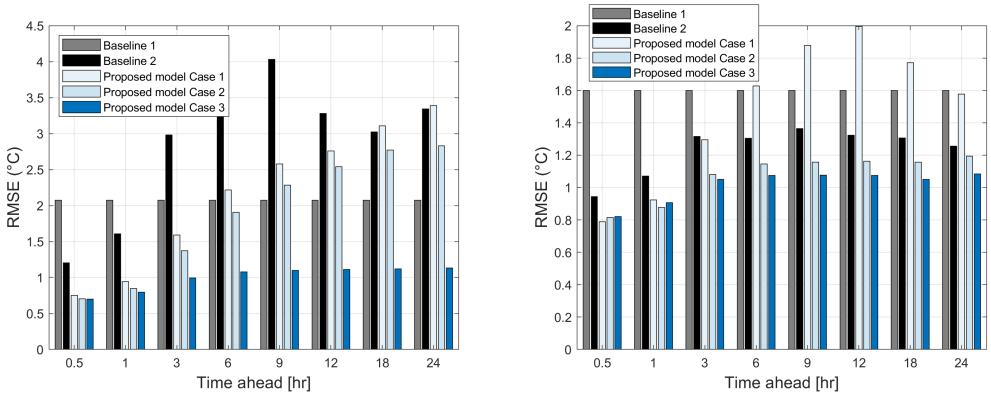

(a) New York

(b) Pittsburgh

Figure 2: Forecast error corresponding to prediction lead time (RSME)

Aug/01/2019 to 00:00 Aug/04/2019 (UTC), which is at least one year apart from the training data. For the different settings on the prediction lead time (00:30, 01:00, 03:00, 06:00, 09:00, 12:00, 18:00, 24:00 ahead), Fig 2 illustrates the prediction error (root mean squared error; RSME) with the various use cases and baselines. In most use cases, the proposed model showed reduced forecast errors than the baselines. On average, Case 3 provides 56% less forecast error than that of Baseline 1 while showing 60% less error, compared to Baseline 2. Reminded that Case 1 and Case 2 use much less information to forecast, the numerical test verifies the proposed model has considerable capacity to predict the short-term surface temperature.

A further investigation is conducted with different error measures. Fig 3 shows the statistical summary of the additional error measures over the target domain using the coefficient of variation in the mean absolute error (CvMAE) and the Pearson linear correlation coefficient (r); the details of the error measures are listed in Malings et al. (2019). Even with the different error measures, the numerical investigation confirms that the proposed model produces an adequate quality of prediction for short-term meso-scale temperature.

5 Heat risk assessment

Finally, we integrate the surrogate model into a framework to assess the urban heat risk. The risk of extreme events is often evaluated by the occurrence rate of the events for the given period. The occurrence rate of a maximum that reaches a threshold at least once during the time interval is often referred to as the first-passage probability. Evaluating the first passage probability is still challenging, but an approximated solution is commonly adopted for most applications. With an assumption of the Poisson arrival for the crossing event, Lutes and Sarkani (1997) and Yi et al. (2019) provides an approximated solution in an analytic form. Fig 4 illustrates the evaluated first passage probability with the threshold 32°C in the New York area. Fig 4 (a) represents the marginal(prior) daily probability over the domain while (b) represents the updated (posterior) probability from 00:00 Aug/02/2020 to 00:00 Aug/04/2020 with the field measurement (until 00:00 Aug/02/2020) and the external 6 hourly forecast (up to 00:00 Aug/04/2020) as in Section 4. For the posterior test period, the highest risk to exceed 32°C is located in Sayreville, New Jersey, with the exceedance probability of 0.4551,

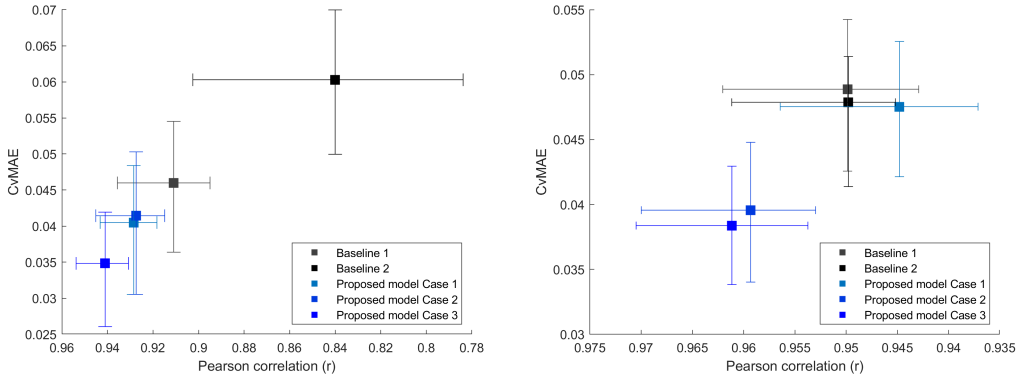

(a) New York (b) Pittsburgh

Figure 3: Summary of statistics of locational forecast error (R vs CvMAE)

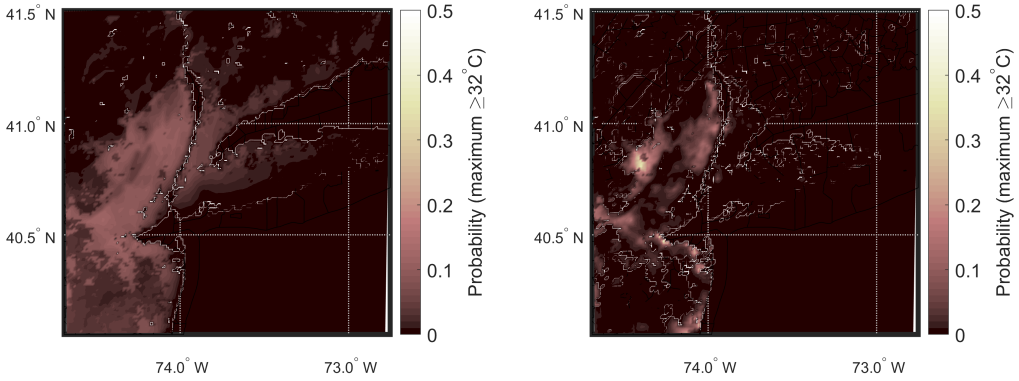

(a) Prior probability (b) Posterior probability

Figure 4: Updated heat risk from 00:00 Aug/02/2020 to 00:00 Aug/04/2020

and its maximum temperature is recorded as 30.18°C according to the test data. This numerical implementation demonstrates how the surrogate model provides advanced insight regarding the heat risk, being integrated with the existing probabilistic risk analysis framework.

We also assess the risk of UHI for the two test domains. In this test, the risk of UHI is considered as the occurrence rate of the maximum temperature gap between the urban areas and the surrounding environments to exceed any threshold during the day (11:00 - 16:00; local time). Fig 5 illustrates the quantified risk of UHI as the exceedance probability curve for the 5 hours of daylight time. The result shows an intensive UHI is more likely to happen at New York than Pittsburgh, during the daylight hours.

6 Conclusion

We developed a surrogate model to forecast short-term meso-scale surface temperature as an alternative to a computationally intensive forecasting system, WRF-PUCM. To forecast surface temperature, Kalman Filter/Smoother based method was implemented. We calibrated the model and tested prediction performance in the domains, around New York and Pittsburgh, for the multiple model-use cases. The numerical test verified that the proposed model produces an adequate quality of prediction at a relatively low computational cost. In the New York domain, the proposed model showed 1.59-0.99°C of 3 hours-ahead prediction error in root-mean-squared error (RMSE), with 0.94-0.95 correlation coefficient (r), depending on model-use scenarios. Similarly, the 3hours-ahead prediction error (RMSE) is measured as 1.30-1.05°C, showing 0.94-0.96 r-value, in the Pittsburgh domain. Finally, we integrate the developed model into a probabilistic risk analysis framework that enables

the surrogate model's advanced usage. The expanded application testifies that the surrogate model can provide a more widened inference on the phenomenon. As results of risk assessment, heat-risk over the domains is evaluated as a map of posterior probability that exceeds extreme temperature for the given period of time, from 00:00 Aug/01/2020 to 00:00 Aug/04/2020, and the occurrence rate of urban heat island is also calculated for both domains. We expect such augmented inference can benefit the public by enabling informed personals and decision-makers to improve community resilience.

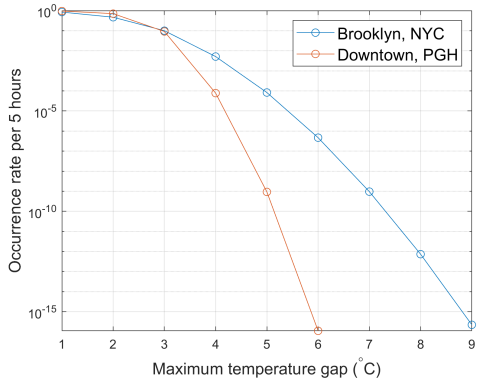

Figure 5: First passage probability curve for the urban heat island

References

[1] B. G. Anderson and M. L. Bell. "Weather-related mortality: how heat, cold, and heat waves affect mortality in the United States". In: *Epidemiology (Cambridge, Mass.)* 20.2 (2009), p. 205.

[2] D. Barber. *Bayesian reasoning and machine learning*. Cambridge University Press, 2012.

[3] L. M. Berliner, C. K. Wikle, and N. Cressie. "Long-lead prediction of Pacific SSTs via Bayesian dynamic modeling". In: *Journal of climate* 13.22 (2000), pp. 3953–3968.

[4] S. A. Changnon, K. E. Kunkel, and B. C. Reinke. "Impacts and responses to the 1995 heat wave: A call to action". In: *Bulletin of the American Meteorological society* 77.7 (1996), pp. 1497–1506.

[5] N. Cressie and C. K. Wikle. *Statistics for spatio-temporal data*. John Wiley & Sons, 2015.

[6] A. Krause, A. Singh, and C. Guestrin. "Near-optimal sensor placements in Gaussian processes: Theory, efficient algorithms and empirical studies". In: *Journal of Machine Learning Research* 9.Feb (2008), pp. 235–284.

[7] D. Li and E. Bou-Zeid. "Quality and sensitivity of high-resolution numerical simulation of urban heat islands". In: *Environmental Research Letters* 9.5 (2014), p. 055001.

[8] L. D. Lutes and S. Sarkani. *Stochastic analysis of structural and mechanical vibrations*. Prentice Hall, 1997.

[9] C. Malings, M. Pozzi, K. Klima, M. Bergés, E. Bou-Zeid, and P. Ramamurthy. "Surface heat assessment for developed environments: Probabilistic urban temperature modeling". In: *Computers, Environment and Urban Systems* 66 (2017), pp. 53–64.

[10] C. Malings, M. Pozzi, K. Klima, M. Bergés, E. Bou-Zeid, and P. Ramamurthy. "Surface heat assessment for developed environments: Optimizing urban temperature monitoring". In: *Building and Environment* 141 (2018), pp. 143–154.

[11] C. Malings, R. Tanzer, A. Hauryliuk, S. P. Kumar, N. Zimmerman, L. B. Kara, A. A. Presto, and R. Subramanian. "Development of a general calibration model and long-term performance evaluation of low-cost sensors for air pollutant gas monitoring". In: *Atmospheric Measurement Techniques* 12.2 (2019), pp. 903–920.

[12] *NCEP North American Mesoscale (NAM) 12 km Analysis*. Boulder CO, 2015. URL: `https://doi.org/10.5065/G4RC-1N91`.

[13] J. A. Voogt and T. R. Oke. "Thermal remote sensing of urban climates". In: *Remote sensing of environment* 86.3 (2003), pp. 370–384.

[14] G. Welch and G. Bishop. *An introduction to the Kalman filter*. Tech. rep. Department of Computer Science, University of North Carolina at Chapel Hill, 1995.

[15] J. A. Weyn, D. R. Durran, and R. Caruana. "Can Machines Learn to Predict Weather? Using Deep Learning to Predict Gridded 500-hPa Geopotential Height From Historical Weather Data". In: *Journal of Advances in Modeling Earth Systems* 11.8 (2019), pp. 2680–2693.

[16] S.-r. Yi, Z. Wang, and J. Song. "Gaussian mixture–based equivalent linearization method (GM-ELM) for fragility analysis of structures under nonstationary excitations". In: *Earthquake Engineering & Structural Dynamics* 48.10 (2019), pp. 1195–1214.